CRYSTAL GROWTH & DESIGN

pubs.acs.org/crystal

Article

New Rubidium-Containing Mixed-Metal Titanium Hollandites

Mohammad Usman, Vancho Kocevski, Mark D. Smith, Gregory Morrison, Theodore Besmann, and Hans-Conrad zur Loye*

Cite This: *Cryst. Growth Des.* 2020, 20, 2398−2405

Read Online

ACCESS | Metrics & More | Article Recommendations | Supporting Information

ABSTRACT: A family of rubidium-containing mixed-metal titanates, $Rb_xM_yTi_{8-y}O_{16}$ (M = Mg, Mn, Fe, Ni, and Cu) was prepared as high-quality single crystals employing a molten RbCl-RbF flux at 850 °C. This is the first report of rubidium-based mixed-metal titanium hollandite materials grown as single crystals. All compounds crystallize in the tetragonal space group *I*4/*m* in the hollandite structure type featuring a three-dimensional framework, composed of mixed Ti/M octahedra, containing square, 2 × 2 tunnels occupied by the Rb cations. Herein, we report on the molten salt-flux crystal growth and solid state synthesis of the phases, the structures of the flux grown crystals, and the magnetic and optical properties of these materials. Magnetization versus temperature measurements for the Fe, Ni, and Cu analogues indicate that all compositions are Curie paramagnets with effective magnetic moments consistent with their respective d-electron count. First-principles calculations in the form of density functional theory were performed to calculate the relative stability, adsorption indexes, and the density of states for select compositions, all of which exhibit stability at 0 K with the computed optical band gaps consistent with the observations.

INTRODUCTION

Titanium dioxide, TiO_2, exists in three different polymorphs, rutile, anatase, and brookite, and finds applications in catalysis,[1] dielectrics,[2] solar cells,[3] photocatalysis,[4] and optics.[5] Another structure type that can be added to the list is hollandite, TiO_2(H),[6] which can be prepared by removing the A cation from the more typical hollandite composition, $A_xM_8O_{16}$. Materials crystallizing in the hollandite structure type with compositions of $A_xM_8O_{16}$[7] are ubiquitous in nature due to their great structural stability and exhibit significant compositional variety as indicated by the presence of alkali, alkaline earth, and even heavy metal cations, such as Pb^{2+}, in these materials.[8−12] Hollandites have the general formula $A_xM_8O_{16}$, where the A site is usually occupied by a large alkali or alkaline earth cation, such as Cs, Sr, or Ba, with the octahedral M site occupied by a single metal cation or by a mixture of these. Hollandite titanates, $A_xTi_8O_{16}$, feature a microporous structure[13] containing 2 × 2 channels that can accommodate a variety of cations as well as small molecules, such as water. These structural features can manifest interesting properties, such as multiferroicity, and suggest a variety of potential applications, such as nuclear waste storage.[14,15]

The presence of the A^{n+} cation in the hollandite tunnels requires mixed valent Ti(III/IV); alternatively, the Ti site can also be shared with a trivalent cation, similar in size to Ti, such as Al^{3+}, or a divalent or trivalent transition metal.[16] The electronic and magnetic properties of the compounds exhibiting the hollandite structure type are directly correlated to the identity and oxidation state of the transition metal and to the position and content of the A site cation.[17,18]

A plethora of Ba-containing Ti-based hollandites are known,[19−21] in contrast to the smaller number of known Na- or K-containing phases.[22−25] Recently, Knyazev et al.[24] for the first time prepared the $M_2Fe_2Ti_6O_{16}$ (M = Na, K, Rb, Cs) family as polycrystalline powders by a conventional solid state route and reported on their thermal expansion coefficients obtained using high-temperature X-ray diffraction. This work demonstrates the ability of the hollandite structure to accommodate larger alkali metals in its channels.[24]

Standard solid state synthesis works well for preparing large quantities of a material, not, however, for preparing single crystals. To that end, molten salt-flux crystal growth can be used as it is an exceptionally versatile technique that utilizes a molten inorganic salt with a relatively low melting point as a high-temperature solvent for crystallization. By employing a unique set of optimized reaction conditions, this method has been shown to produce a myriad of complex oxides with intriguing properties.[26−29] Using a mixed RbCl-RbF melt, we report on the synthesis of the first rubidium-containing mixed metal titanates, $Rb_xM_yTi_{8-y}O_{16}$ (M = Mg, Mn, Fe, Ni, and Cu), grown as high-quality single crystals. In addition, the

Received: November 21, 2019
Revised: January 28, 2020
Published: March 3, 2020

oxyfluoride $Rb_{1.50}Ti_{7.26}O_{14.41}F_{1.59}$ was also serendipitously obtained in an attempt to crystallize the Cr analogue of the family. All title compounds crystallize in the tetragonal space group $I4/m$ in the hollandite structure type. Density functional theory (DFT) calculations were utilized to obtain absorption indexes, density of states (DOS), and thus the stability of select compositions.

EXPERIMENTAL SECTION

Methods and Materials. $MgCl_2$ (Fisher Scientific), $CrCl_3{\cdot}6H_2O$ (99%, MCB), MnF_3 (98%, Alfa Aesar), FeF_3 (99%, Strem), NiF_2 (99%, Alfa Aesar), CuF_2 (99.5%, Alfa Aesar), Fe_2O_3 (99.5%, Alfa Aesar), NiO (99.995%, BTC), CuO (99.99%, Aldrich), TiO_2-rutile (99.9%, Alfa Aesar), RbCl (99%, Alfa Aesar), RbF (99.1%, Alfa Aesar), and Rb_2CO_3(99%, Alfa Aesar) were used for the flux growth synthesis and solid state synthesis.

Crystal Growth. All title compositions were prepared by layering a mixture of 1 mmol of $MgCl_2$ or the appropriate transition metal fluoride precursor and 1 mmol of TiO_2 beneath a mixture of 1.34 g of RbCl and 1.02 g of RbF in a 7.5 cm tall by 1.2 cm diameter cylindrical silver crucible with one of its ends sealed and welded shut. The other end of the crucible containing the charge was crimped shut, and the loaded crucible was placed into a programmable furnace. The reaction mixture was heated at 10 °C/min to 850 °C, maintained at this temperature for 12 h, slow cooled at 6−10 °C/h to 400 °C, and then rapidly cooled to room temperature by shutting the furnace off. Once cooled to ambient temperature, the solidified RbCl-RbF flux was dissolved in distilled hot water, aided by sonication, and the resulting products were isolated via vacuum filtration. All compositions formed as thin, plate-like crystals (approximate dimensions 0.15 × 0.03 × 0.02 mm^3) in less than 20% yield. An optical image of single crystals of the Fe analogue is provided in Figure 1.

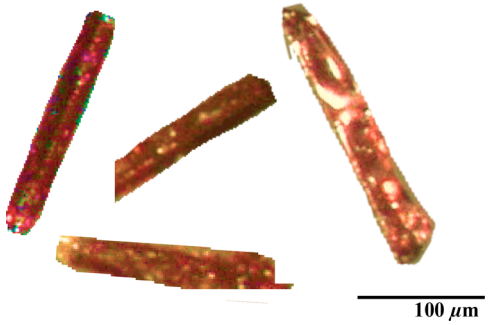

Figure 1. Optical image of $Rb_{1.66}Fe_{1.66}Ti_{6.34}O_{16}$ single crystals.

Solid State Synthesis. Polycrystalline samples were synthesized by using stoichiometric amounts of Rb_2CO_3 and TiO_2 as well as Fe_2O_3, NiO, and CuO for the Fe, Ni, and Cu analogues, respectively. For each reaction, the starting materials were mixed in an agate mortar and pestle and then loaded into an alumina crucible previously thoroughly cleaned in aqua regia and oven-dried. The charge was heated at 10 °C/min to 400 °C, maintained at this temperature for 24 h, and then ramped at 10 °C/h to 900 °C, maintained at this temperature for 24 h, whereupon the furnace was shut off and allowed to cool to room temperature naturally. Multiple grindings and subsequent heat treatments at 975 °C led to the formation of phase-pure polycrystalline products in all three cases. Synthesis of the Mn analogue was attempted using Mn_2O_3, TiO_2, and Rb_2CO_3; however, despite changing the reaction profile and increasing the dwell time, a phase pure sample could not be prepared as evidenced by several strong unmatched reflections in the powder pattern.

Single Crystal X-ray Diffraction. For all title compositions, X-ray intensity data from a suitable crystal were collected at 301(2) K using a Bruker D8 QUEST diffractometer equipped with a PHOTON 100 CMOS area detector and an Incoatec microfocus source (Mo Kα radiation, λ = 0.71073 Å).[30] The raw area detector data frames were reduced and corrected for absorption effects using the SAINT+ and SADABS programs.[30,31] Final unit cell parameters were determined by least-squares refinement of a large array of reflections taken from the data set. An initial structural model was obtained with SHELXT. Subsequent difference Fourier calculations and full-matrix least-squares refinement against F^2 were performed with SHELXL-2018[32] using the ShelXle interface.[33] Details of the structure solution process for each phase can be found in the Supporting Information. Crystallographic refinement data for all title compounds are listed in Table 1.

Powder X-ray Diffraction (PXRD). Powder X-ray diffraction data were collected on a Bruker D2 Phaser using Cu Kα radiation (λ = 1.54018 Å) and equipped with a LYNXEYE silicon strip detector. The scan covered the angular range 10−70° in steps of 0.02°. The experimental and calculated PXRD patterns are in good agreement and are provided as Figures S1−S3.

Energy Dispersive Spectroscopy (EDS). Semiquantitative elemental analysis was carried out using a TESCAN Vega-3 SBU scanning electron microscope (SEM) with EDS capabilities. The crystals were mounted on carbon tape, and analysis was carried out using a 20 kV accelerating voltage and an accumulation time of 20 s. EDS verified the presence of the appropriate elements in each single crystal. Additionally, the absence of extraneous elements such as silver from the reaction vessel was confirmed within the detection limits of the instrument. Select EDS and SEM results are provided in Table S1.

Optical Properties. UV−vis diffuse reflectance spectroscopy data were collected on polycrystalline samples of the Fe, Ni, and Cu analogues using a PerkinElmer Lambda 35 UV−vis scanning spectrophotometer equipped with an integrating sphere in the range of 200−900 nm. The reflectance data were converted to absorbance data using the Kubelka−Munk function.[34] Infrared spectroscopy was performed using a PerkinElmer spectrum 100 FT-IR spectrometer with a diamond ATR attachment. IR spectra were recorded in the spectral range of 4000 cm^{-1} to 650 cm^{-1}. Final IR spectra consisted of 16 total averaged scans.

Magnetic Susceptibility. Magnetic properties were measured on polycrystalline samples of the Fe, Ni, and Cu analogues using a Quantum Design Magnetic Properties Measurement System (QD MPMS 3 SQUID Magnetometer). Magnetic susceptibility was measured under zero-field cooled (zfc) and field cooled (fc) conditions from 2 to 300 K at applied field of 0.1 T. Magnetization as a function of field was measured from −5 to 5 T at 2 K. Data were corrected for sample shape and radial offset effects as described previously.[35] The zfc and fc data completely overlapped, and therefore only the zfc data are provided.

First-Principles Calculations. First-principles calculations, in the form of DFT, were performed using the Vienna Ab-initio Package (VASP) code,[36,37] the generalized gradient approximation of Perdew, Burke and Ernzerhof (PBE), and the projector augmented wave (PAW) method.[38−40] To model the mixing and partial occupies in the studied compounds, super quasi-random structures (SQSs) were generated using the mcsqs code provided by the Alloy Theoretic Automated Toolkit (ATAT),[41−44] with each composition close to the experimentally determined composition: $Rb_{1.67}Fe_{1.67}Ti_{6.33}O_{16}$, $Rb_{1.6}Ni_{0.8}Ti_{7.2}O_{16}$, and $Rb_{1.6}Cu_{0.8}Ti_{7.2}O_{16}$. To determine if the compounds are thermodynamically stable, i.e., if they break the respective Rb−M−Ti−O (M = Fe, Ni, Cu) convex hulls, their formation energies were compared with those generated in the Open Quantum Materials Database (OQMD).[45,46] The following OQMD conditions were used: 520 eV cutoff energy for the plane wave basis set, 10^{-4} eV energy convergence criterion, 4 × 2 × 2 and 4 × 4 × 3 k-point meshes for the $Rb_{1.67}Fe_{1.67}Ti_{6.33}O_{16}$ and $Rb_{1.6}M_{0.8}Ti_{7.2}O_{16}$ (M = Ni, Cu) compounds, respectively, and U_{eff} = 5.3, 6.4, and 4.0 eV for the Fe, Ni, and Cu atoms, respectively. The systems were considered to be spin-polarized, with ferromagnetic ordering of the Fe, Ni, and Cu atoms. For calculating the electronic and optical properties, more rigorous calculations were performed using a 520 eV cutoff energy for the plane wave basis set; 10^{-6} eV and 10^{-3} eV/Å energy and forces convergence criteria, respectively; and the same k-point meshes as the

https://dx.doi.org/10.1021/acs.cgd.9b01560
Cryst. Growth Des. 2020, 20, 2398−2405

Table 1. Crystallographic and Structure Refinement Data for All Title Compositions

empirical formula	$Rb_{1.48}Mg_{0.74}Ti_{7.26}O_{16}$	$Rb_{1.50}Ti_{7.26}F_{1.59}O_{14.41}$	$Rb_{1.44}Mn_{3.03}Ti_{4.97}O_{16}$	$Rb_{1.66}Fe_{1.66}Ti_{6.34}O_{16}$	$Rb_{1.56}Ni_{0.78}Ti_{7.22}O_{16}$	$Rb_{1.54}Cu_{0.77}Ti_{7.23}O_{16}$
formula weight	758.38	736.18	783.78	794.05	780.68	782.62
crystal system and space group	tetragonal $I4/m$					
crystal color and habit	colorless block	yellow rod	black rod	orange needle	yellow rod	yellow rod
a (Å)	10.2012(15)	10.1817(6)	10.128(2)	10.1836(8)	10.1914(3)	10.1904(3)
c (Å)	2.9697(5)	2.9567(2)	2.9138(7)	2.9729(2)	2.96440(8)	2.97104(8)
V (Å^3)	309.04(10)	306.51(4)	298.89(15)	308.31(5)	307.895(17)	308.525(18)
ρ_{calc} (g/cm^3)	4.021	3.988	4.354	4.277	4.210	4.212
radiation (λ, Å)	Mo K_α (0.71073)					
μ (mm^{-1})	10.379	10.486	12.166	12.377	11.806	11.850
T (K)	301 (2)					
crystal size (mm^3)	0.14 × 0.12 × 0.10	0.80 × 0.40 × 0.30	0.80 × 0.20 × 0.20	0.80 × 0.30 × 0.20	0.18 × 0.06 × 0.04	0.18 × 0.14 × 0.08
θ range (deg)	2.824−45.054	2.829−37.732	2.844−35.006	2.829−36.313	2.827−35.166	2.827−36.341
goodness of fit	1.206	1.117	1.114	1.238	1.159	1.204
R_1 ($I > 2\sigma(I)$)	0.0136	0.0156	0.0140	0.0118	0.0133	0.0122
wR_2 (all data)	0.0348	0.0388	0.0303	0.0343	0.0311	0.0294
largest peak and hole (e$^-$/Å^3)	0.452/-0.447	0.636/-0.308	0.291/-0.372	0.288/-0.345	0.269/-0.292	0.320/-0.295

OQMD calculations. The ground state geometries were obtained by relaxing the cell volume, cell shape, and atomic positions. The adsorption indexes were obtained from the calculated frequency dependent dielectric function in the independent-particle picture.

RESULTS AND DISCUSSION

Alkali Halide Flux Growth. The ability of molten alkali halides to dissolve a rather extensive list of binary reagents, such as simple transition metal oxides and fluorides, main group oxides, and alkaline earth carbonates, makes the alkali halide fluxes very effective for crystallizing a large variety of oxide structure types with diverse compositions.[47] Although most materials can be crystallized from a number of fluxes, it has been established empirically that some fluxes are more effective than others for obtaining particular classes of materials.[48,49] Fluoride melts, for example, can readily dissolve oxide reagents because the fluoride ion can act as a mineralizer, enhancing solubility. For complex oxides, such as the hollandites presented herein, alkali fluoride or mixed fluoride-chloride fluxes are extremely effective for producing high-quality single crystals in good yield, and we have not found a flux that provided us with superior results.

For the hollandite crystal growth, a fluoride component is necessary to dissolve the titanium precursor, TiO_2, which does not readily dissolve in simple chloride melts at temperatures less than 850 °C. For example, the $K_x(Ti,M)_8O_{16}$ (M = Sc − Ni) compounds reported by the Rodriguez group were prepared by soaking mixtures of precalcined transition metal oxide and TiO_2 in a molten KCl + KNO_3 salt mixture at temperatures ranging from 1200−1300 °C for 36 h.[22] In contrast to this, the use of mixed alkali halide melts enabled us to prepare the title phases at 850 °C, a substantially lower temperature. The crystal growth utilized transition metal fluoride reagents as they dissolve rapidly in the mixed halide melts and readily yielded X-ray quality crystals of manganese, iron, nickel, and copper containing hollandite phases. On the other hand, all attempts at obtaining a Cr-based hollandite failed, in spite of trying different chromium reagents and modifying the reaction profile. These reactions, however, resulted in the serendipitous formation of an oxyfluoride phase, $Rb_{1.50}Ti_{7.26}F_{1.59}O_{14.41}$. As the introduction of fluoride ions into the hollandite structure represents a potential approach for tuning the band gap of these materials, we are planning to pursue this in future investigations. Interestingly, none of the other reactions showed any signs of oxyfluoride products, and no oxyfluoride species were detected by single crystal X-ray diffraction or EDS measurements. Flux synthesis using a small alkaline earth, Mg, led to formation of the desired Mg-based hollandite in addition to a minor quantity of a rubidium magnesium fluoride perovskite impurity, $RbMgF_3$. Attempts to exchange rubidium cations in the Ni and Cu hollandites with a smaller alkali cation, such as Na or K, by soaking their single crystals in a molten ANO_3 (A = Na, K) salt, were unsuccessful.

Crystal Structure. All title compounds crystallize in the tetragonal space group $I4/m$. The crystal growth mechanism for a potassium hollandite, $K_{1.46}Fe_{0.8}Ti_{7.2}O_{16}$, has been discussed in detail by Hassan et al.[25] Similar arguments can be made for the rubidium hollandites; briefly, the TiO_2 undergoes dissolution in molten RbCl-RbF flux presumably forming structural building blocks of TiO_6^{8-} octahedra. The transition metal cations, once dissolved in the flux, connect to the TiO_6^{8-} building blocks to occupy Ti sites due to the nearly identical ionic radii of Ti^{4+} and M^{x+}, for example, 0.64 and 0.61 Å for Fe^{3+} and Ti^{4+} ions, respectively. This similarity in ionic radii leads to the substitution of transition metal cations for titanium in the mixed metal rubidium phases. Figure 2 illustrates the local coordination environments of the hollandite elements. A depiction of the relationship between the TiO_2 rutile structure and the idealized Ti_8O_{16} hollandite structure is shown in Figure 3.

The formation of single crystals of our series of rubidium phases in the tetragonal hollandite structure type is consistent with the report on the solid state synthesis and structural characterization of $M_2Fe_2Ti_6O_{16}$ (M = Na, K, Rb, Cs) series by

https://dx.doi.org/10.1021/acs.cgd.9b01560
Cryst. Growth Des. 2020, 20, 2398−2405

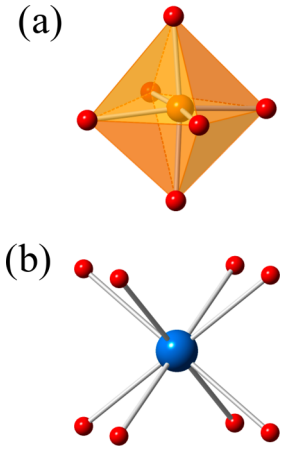

Figure 2. (a) Local coordination environment of the mixed-metal M site and (b) the Rb^+ cation in the $Rb_xM_yTi_{8-y}O_{16}$ hollandite structure.

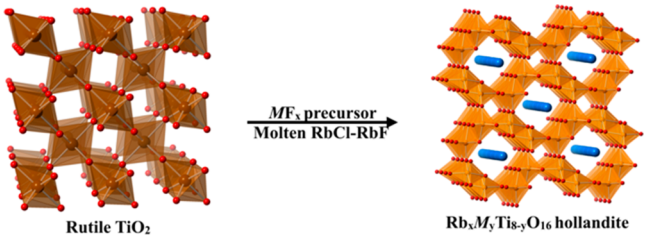

Figure 3. Depiction of how the $Rb_{1.66}Fe_{1.66}Ti_{6.34}O_{16}$ hollandite (shown to the right of the arrow) is related to the rutile phase of TiO_2 (shown to the left of the arrow). Ti in TiO_2 is shown in brown, and the mixed Ti/Fe metal centers in $Rb_{1.66}Fe_{1.66}Ti_{6.34}O_{16}$ are shown in orange. O and Rb are shown as red and blue spheres, respectively.

Knyazev et al.,[24] who found that the Li phase crystallizes in the spinel structure, the Na phase in the monoclinic freudenbergite structure, and the rubidium and cesium phases both in the tetragonal hollandite structure.

The crystal structure of the Rb−M−Ti−O hollandites consists of mixed-metal octahedra that corner- and edge-share using O(1) and O(2) respectively resulting in the formation of a three-dimensional $[M_xTi_{8-x}O_{16}]^{y-}$ framework featuring 2 × 2 or square-shaped tunnels that run down the crystallographic *c*-axis. These channels are occupied by the disordered rubidium cations that are arranged in a nearly continuous line along the *c* axis [0, 0, *z*] and that provide charge balance to compensate for the presence of the 2+ or 3+ cation in place of the Ti^{4+} cation in the framework. The M−O (M = Mg, Ti, Mn, Fe, Ni, and Cu) interatomic distances are provided in Table 2.

Optical Properties. The reflectance data for the Fe, Ni and Cu analogues are presented in Figure 4. For the Fe complex, the two optical absorption edges, E_{g1} = ∼1.90 eV and E_{g2} = ∼2.20 eV, obtained by the intercept of the extrapolated line to the energy (eV) axis, are ligand to metal or O^{2-} to Ti^{4+} (Fe^{3+})

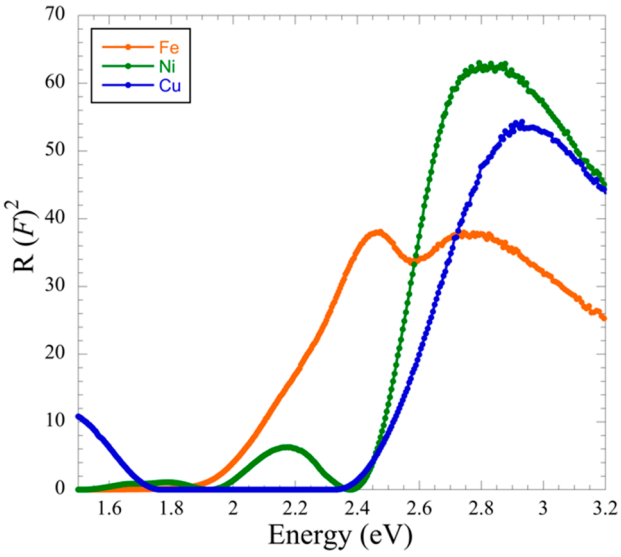

Figure 4. Tauc plots for $Rb_xM_yTi_{8-y}O_{16}$ (M = Fe, Ni, and Cu) obtained from the UV−vis diffuse reflectance data.

charge transfer bands, as shown by the projected DOS around the band gap transition energies in Figure 7. These charge transfer energy values are close to the band gap transition energies obtained from DFT for the spin-up and spin-down channels, respectively. The absorption edges for the Ni and Cu complexes are situated at E_g = ∼2.45 eV and E_g = ∼2.35 eV respectively. These can be attributed to the charge transfer between Ni-3d or Cu-3d to Ti-3d, or between the intermediate bands, that arise from the lower chemical potential of the transition metals with respect to those of Ti, to the conduction band. The FT-IR spectra collected on polycrystalline Fe, Ni, and Cu analogues are provided in Figure 5. In all three cases, a sharp band, close to 760 cm^{-1}, can be observed. This is attributed to the stretching modes of the mixed Ti/M octahedra in the materials. This value is in an excellent agreement with the value reported for $K_{1.46}Fe_{0.8}Ti_{7.2}O_{16}$.[28]

Magnetic Properties. Figure 6 shows the temperature dependent magnetic susceptibility data for the Fe, Ni, and Cu analogues, and the magnetic data are summarized in Table 3. No magnetic order is observed in any of the analogues down to 2 K. Fitting the high-temperature (50−300 K) susceptibilities to a modified Curie−Weiss law, $\chi = \chi_o + C/(T - \theta)$, where χ_o is a temperature independent term, results in effective moments of 4.27(2) μ_B/Fe, 2.98(2) μ_B/Ni, and 1.85(2) μ_B/Cu for Fe^{3+}, Ni^{2+}, and Cu^{2+} ions, respectively. The Ni and Cu magnetic moments are slightly higher than the calculated spin only moments, 2.83 μ_B/Ni and 1.73 μ_B/Cu, but are in good agreement with their range of typically observed moments that result from partial spin−orbit coupling.[50] The observed moment for $Rb_{1.66}Fe_{1.66}Ti_{6.34}O_{16}$, 4.27(2) μ_B/Fe, is considerably lower than the calculated and typically observed

Table 2. Interatomic Distances for All Title Compositions

	Mg	Ti	Mn	Fe	Ni	Cu
M−O (1)	1.9356(5)	1.9361(8)[a]	1.9474(10)	1.9305(8)	1.9318(7)	1.9325(8)
M−O (1) × 2	1.9769(4)	1.9681(6)	1.9303(7)	1.9712(5)	1.9737(5)	1.9743(5)
M−O (2) × 2	1.9676(4)	1.9637(6)	1.9478(7)	1.9798(5)	1.9709(5)	1.9730(5)
M−O (2)	2.0200(5)	2.0165(9)	2.0061(11)	2.0183(8)	2.0205(7)	2.0166(8)

[a]O (1) is a mixed O/F (80/20) site.

https://dx.doi.org/10.1021/acs.cgd.9b01560
Cryst. Growth Des. 2020, 20, 2398−2405

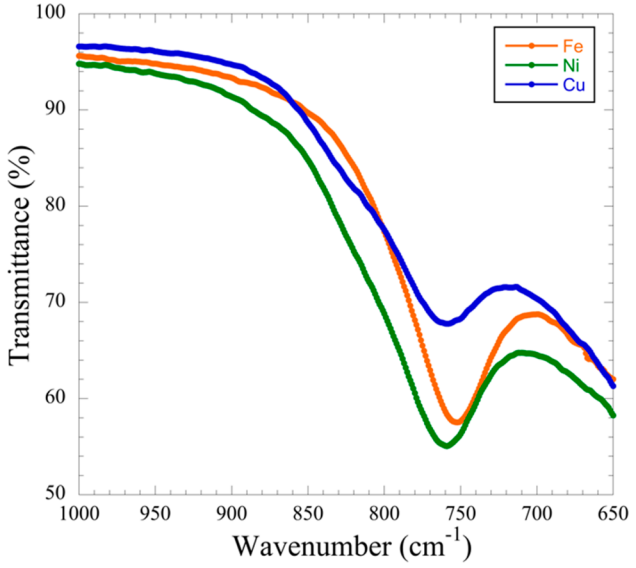

Figure 5. FT-IR spectra for $Rb_xM_yTi_{8-y}O_{16}$ (M = Fe, Ni, and Cu) indicating a broad stretch at ~760 cm^{-1} characteristic of the stretching modes of the $(Ti/M)O_6$ octahedra.

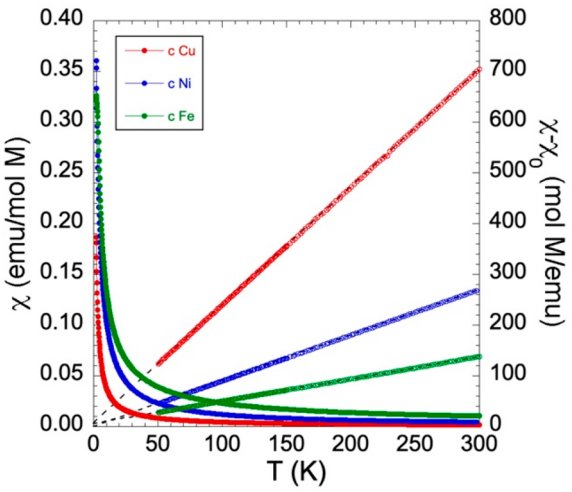

Figure 6. Temperature dependent susceptibility and the fit region of the inverse magnetic susceptibility for $Rb_xM_yTi_{8-y}O_{16}$ (M = Fe, Ni, and Cu). Data collected at H = 0.1 T. Curie–Weiss fits to a modified Curie–Weiss law are shown as dashed lines.

moment of 5.92 μ_B/Fe for high-spin Fe(III). As neither PXRD nor EDS data indicated any impurity in the sample and the Fe concentration is fixed by the solid-state synthesis, this strongly suggests that the reduced Fe moment is intrinsic to $Rb_{1.66}Fe_{1.66}Ti_{6.34}O_{16}$. A similarly reduced moment was observed in $Ba_3FeRu_2O_9$, which consists of mixed Fe/Ru in isolated octahedra and octahedral dimers, and was suggested to possibly arise due to clustering of iron in the structure.[51,52] The magnetization versus field (MvH) plots for all three compounds are provided in Figure S4 and are typical of paramagnetic compounds.

First-Principles Calculations. The DFT calculations showed that the Fe and Cu analogues break their respective OQMD convex hulls by 0.31 and 0.56 kJ/mol, indicating that these compounds are energetically stable. Although the Ni analogue is 0.3 kJ/mol above the Rb–Ni–Ti–O convex hull, the energy difference is very small such that a small increase in temperature (36 K) could stabilize this compound. The band gaps in the spin-up channel for the Fe, Ni, and Cu analogues are 2.37, 2.49, and 2.34 eV, respectively, while the band gaps in the spin-down show some larger dissimilarity, being 2.55, 2.67, and 1.58 eV for the Fe, Ni, and Cu analogues, respectively. The inconsistency in the spin-up and spin-down channel band gaps comes from the different contribution from the metals to the states around the band gap, which can be seen from the PDOS (Figure 7). In general, the PDOS of the Fe, Ni, and Cu analogues are very similar, where the O states dominate the valence band maximum (VMB) and the Ti states the conduction band minimum (CBM), with a small contribution from the metals in the spin-up channel. There are Fe states at the CBM in the spin down channel of the Fe analogues, which is not the case for the Ni analogue, where Ti states dominated the CBM in spin-up and spin-down channel. In the case of the Cu analogue, the states around the smaller band gap in the spin-down channel are dominated by Cu states, and to a lesser extent by O states, indicating that the initial adsorption edge comes from Cu–Cu transitions. Also, unlike the other analogues, in the Cu analogue spin-down channel there is a gap between the VBM and the other VB states, as well as a gap between the CBM and the other CB states. The smaller band gap in the spin-down channel and the gap between VBM and CBM with the rest of the states can explain the peak at 1.6 eV and the gap between 1.7 and 2.4 eV in the experimental adsorption index of the Cu analogue. The adsorption indexes also reflect the dissimilarity in the PDOS around the band gap, with the adsorption indexes at energies <3.2 eV being somewhat different. At energies >3.2 eV, the transition from O^{2-} to Ti^{4+} and from M^{n+} to O^{2-} are dominating, generating similar adsorption indexes.

CONCLUSION

A family of rubidium-containing transition metal hollandites was synthesized via molten RbCl-RbF flux crystal growth. Single crystal structures for all title compounds were solved by single crystal X-ray diffraction. All members of the family crystallize in the tetragonal space group $I4/m$. Optical properties for the Fe, Ni, and Cu containing analogues were measured by UV–vis spectroscopy and FT-IR spectroscopy. Magnetic property measurements for these materials showed that they are simple paramagnets in the 2–300 K range. The transitions at the band gap in the adsorption indexes of Ni and Cu analogues are corroborated by the calculated PDOS, and

Table 3. Magnetic Properties for $Rb_xM_yTi_{8-y}O_{16}$ (M = Fe, Ni, and Cu)

compound	H (T)	fit range (K)	χ (emu/mol M)	θ_w (K)	μ_{eff} (μ_B/M)	μ_{calc} (μ_B/M)[a]	spin state
$Rb_{1.66}Fe_{1.66}Ti_{6.34}O_{16}$	0.1	50–300	0.0031	−13.9(3)	4.27(2)	5.92	d^5 - high-spin
$Rb_{1.56}Ni_{0.78}Ti_{7.22}O_{16}$	0.1	50–300	0.00082	0.0(3)	2.98(2)	2.83	d^8
$Rb_{1.54}Cu_{0.77}Ti_{7.23}O_{16}$	0.1	50–300	0.00027	−3.1(3)	1.85(2)	1.73	d^9

[a]Moment calculated from spin-only values.

https://dx.doi.org/10.1021/acs.cgd.9b01560
Cryst. Growth Des. 2020, 20, 2398–2405

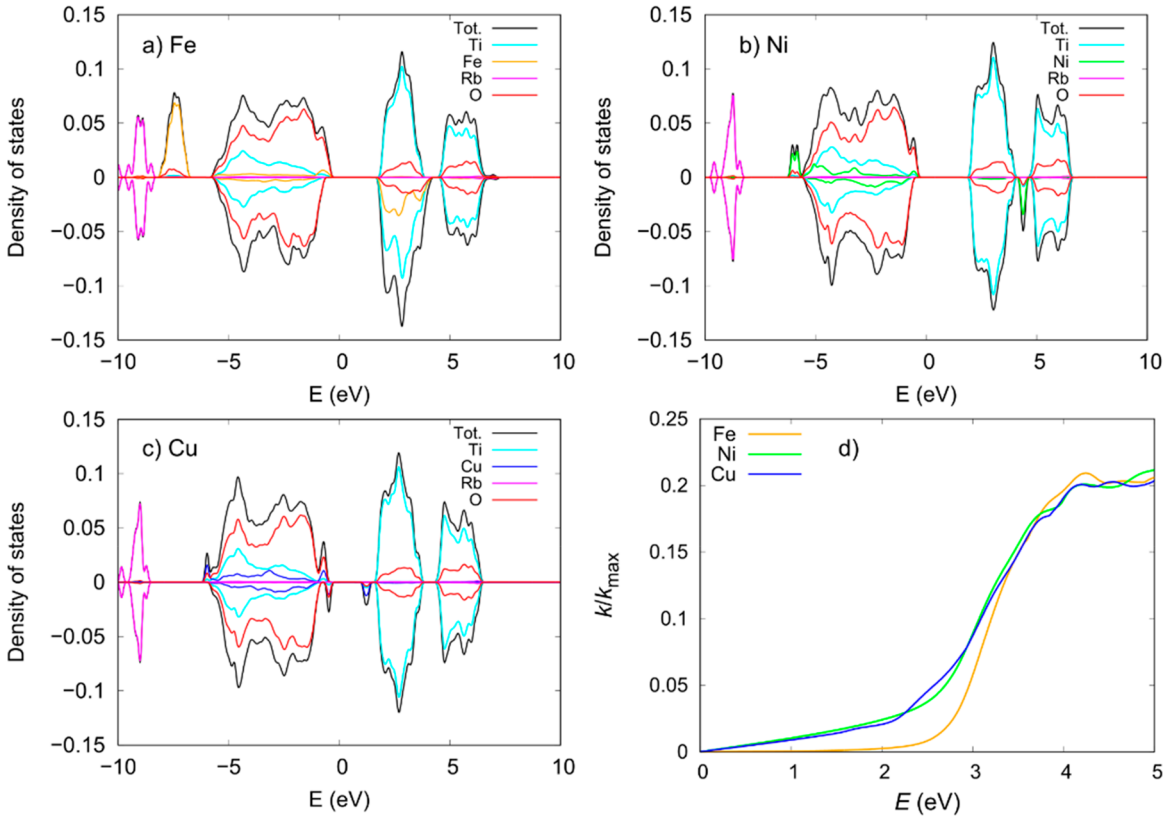

Figure 7. Projected density of states (PDOS) of (a) Fe, (b) Ni, and (c) Cu analogues. (d) Adsorption indexes of the Fe, Ni, and Cu analogues. The spin-up and spin-down channels are shown as positive and negative DOS, respectively.

moreover, the calculations give further explanation of the origin of the observed two band gaps in the Fe analogue. Additionally, for all three analogues, the adsorption at energies higher than 3.2 eV come from M^{n+} to O^{2-}, giving rise to similar adsorption indexes.

■ ASSOCIATED CONTENT

Supporting Information

The Supporting Information is available free of charge at https://pubs.acs.org/doi/10.1021/acs.cgd.9b01560.

Optical images, EDS and SEM results, PXRD patterns for the Fe, Ni, and Cu hollandites, and details of structure solution (PDF)

Accession Codes

CCDC 1895741, 1958928−1958931, and 1959203 contain the supplementary crystallographic data for this paper. These data can be obtained free of charge via www.ccdc.cam.ac.uk/data_request/cif, or by emailing data_request@ccdc.cam.ac.uk, or by contacting The Cambridge Crystallographic Data Centre, 12 Union Road, Cambridge CB2 1EZ, UK; fax: +44 1223 336033.

■ AUTHOR INFORMATION

Corresponding Author

Hans-Conrad zur Loye − *Department of Chemistry and Biochemistry, University of South Carolina, Columbia, South Carolina 29208, United States*; Phone: (803) 777-6916; Email: zurloye@mailbox.sc.edu; Fax: (803) 777-8508

Authors

Mohammad Usman − *Department of Chemistry and Biochemistry, University of South Carolina, Columbia, South Carolina 29208, United States*; orcid.org/0000-0002-9791-4364

Vancho Kocevski − *Department of Mechanical Engineering, University of South Carolina, Columbia, South Carolina 29208, United States*; orcid.org/0000-0002-2127-5834

Mark D. Smith − *Department of Chemistry and Biochemistry, University of South Carolina, Columbia, South Carolina 29208, United States*; orcid.org/0000-0001-6977-7131

Gregory Morrison − *Department of Chemistry and Biochemistry, University of South Carolina, Columbia, South Carolina 29208, United States*; orcid.org/0000-0001-9674-9224

Theodore Besmann − *Department of Mechanical Engineering, University of South Carolina, Columbia, South Carolina 29208, United States*; orcid.org/0000-0001-5598-0550

Complete contact information is available at: https://pubs.acs.org/10.1021/acs.cgd.9b01560

Notes

The authors declare no competing financial interest.

■ ACKNOWLEDGMENTS

M.U., M.D.S., G.M., and H.Z.L. gratefully acknowledge the U.S. National Science Foundation, Award OIA-1655740, for supporting the crystal growth, synthesis, and structure determination efforts. V.K. and T.M.B. acknowledge the support by the U.S. Department of Energy, Office of Science, Basic Energy Sciences, under Award No. DE-SC0016574

(Center for Hierarchical Waste Form Materials) for supporting the computational efforts. This research used computational resources provided by the National Energy Research Scientific Computing Center (NERSC) and the HPC cluster Hyperion, supported by The Division of Information Technology at the University of South Carolina.

REFERENCES

(1) Hashimoto, K.; Irie, H.; Fujishima, A. TiO_2 Photocatalysis: A Historical Overview and Future Prospects. *Jpn. J. Appl. Phys.* **2005**, *44*, 8269−8285.
(2) Campbell, S. A.; Gilmer, D. C.; Wang, X. C.; Hsieh, M. T.; Kim, H. S.; Gladfelter, W. L.; Yan, J. H. MOSFET transistors fabricated with high permitivity TiO_2 dielectrics. *IEEE Trans. Electron Devices* **1997**, *44*, 104−109.
(3) O'Regan, B.; Gratzel, M. A low-cost, high-efficiency solar cell based on dye-sensitized colloidal TiO_2 films. *Nature* **1991**, *353*, 737−740.
(4) Maeda, K. Rhodium-Doped Barium Titanate Perovskite as a Stable p-Type Semiconductor Photocatalyst for Hydrogen Evolution under Visible Light. *ACS Appl. Mater. Interfaces* **2014**, *6*, 2167−2173.
(5) Bange, K.; Ottermann, C. R.; Anderson, O.; Jeschkowski, U.; Laube, M.; Feile, R. Investigations of TiO_2 films deposited by different techniques. *Thin Solid Films* **1991**, *197*, 279−285.
(6) Pérez-Flores, J. C.; Baehtz, C.; Kuhn, A.; García-Alvarado, F. Hollandite-type TiO_2: A New Negative Electrode Material for Sodium-Ion Batteries. *J. Mater. Chem. A* **2014**, *2* (6), 1825−1833.
(7) Byström, A.; Byström, A. M. The Crystal Structure of Hollandite, the Related Manganese Oxide Minerals, and α-MnO_2. *Acta Crystallogr.* **1950**, *3* (2), 146−154.
(8) Bevara, S.; Achary, S. N.; Garg, N.; Chitnis, A.; Sastry, P. U.; Shinde, A. B.; Krishna, P. S. R.; Tyagi, A. K. Pressure and Temperature Dependent Structural Studies on Hollandite Type Ferrotitanate and Crystal Structure of a High Pressure Phase. *Inorg. Chem.* **2018**, *57*, 2157−2168.
(9) Miura, H.; Iura, H. The crystal structure of hollandite. *Mineral. J.* **1986**, *13*, 119−129.
(10) Reguir, E. P.; Chakhmouradian, A. R.; Mitchell, R. H. Pb-bearing hollandite-type titanates: A first natural occurrence and reconnaissance synthesis study. *Mineral. Mag.* **2003**, *67*, 957−965.
(11) Cheary, R. W. An analysis of the structural characteristics of hollandite compounds. *Acta Crystallogr., Sect. B: Struct. Sci.* **1986**, *42*, 229−236.
(12) Vasconcelos, P. M.; Renne, P. R.; Brimhall, G. H.; Becker, T. A. Direct dating of weathering phenomena by 40Ar/39Ar and K-Ar analysis of supergene K-Mn oxides. *Geochim. Cosmochim. Acta* **1994**, *58*, 1635−1665.
(13) Vogt, T.; Schweda, E.; Wustefeld, C.; Strahle, J.; Cheetham, A. K. Structural analysis of a potassium hollandite $K_{1.35}Ti_8O_{16}$. *J. Solid State Chem.* **1989**, *83*, 61−68.
(14) Wen, Y.; Xu, Y.; Brinkman, K. S.; Shuller-Nickles, L. Atomistic scale investigation of cation ordering and phase stability in Cs-substituted $Ba_{1.33}Zn_{1.33}Ti_{6.67}O_{16}$, $Ba_{1.33}Ga_{2.66}Ti_{5.67}O_{16}$ and $Ba_{1.33}Al_{2.66}Ti_{5.33}O_{16}$ hollandite. *Sci. Rep.* **2018**, *8*, 5003.
(15) Liu, S.; Akbashev, A. R.; Yang, X.; Liu, X.; Li, W.; Zhao, L.; Li, X.; Couzis, A.; Han, M. G.; Zhu, Y.; Krusin-Elbaum, L.; Li, J.; Huang, L.; Billinge, S. J.; Spanier, J. E.; O'Brien, S. Hollandites as a new class of multiferroics. *Sci. Rep.* **2015**, *4*, 6203.
(16) Moetakef, P.; Wang, L.; Maughan, A. E.; Gaskell, K. J.; Larson, A. M.; Hodges, B. C.; Rodriguez, E. E. Tuning the electronic band structure of microporous titanates with the hollandite structure. *J. Mater. Chem. A* **2015**, *3*, 20330−20337.
(17) Isobe, M.; Koishi, S.; Kouno, N.; Yamaura, J.-I.; Yamauchi, T.; Ueda, H.; Gotou, H.; Yagi, T.; Ueda, Y. Observation of Metal-Insulator Transition in Hollandite Vanadate, $K_2V_8O_{16}$. *J. Phys. Soc. Jpn.* **2006**, *75*, 073801.
(18) Lebedev, O. I.; Hébert, S.; Roddatis, V.; Martin, C.; Turner, S.; Krasheninnikov, A. V.; Grin, Y.; Maignan, A. Revisiting Hollandites: Channels Filling by Main-Group Elements Together with Transition Metals in $Bi_{2-y}V_yV_8O_{16}$. *Chem. Mater.* **2017**, *29*, 5558−5565.
(19) Cheary, R. W. An Analysis of the Structural Characteristics of Hollandite Compounds. *Acta Crystallogr., Sect. B: Struct. Sci.* **1986**, *42*, 229−236.
(20) Carter, M. L. Tetragonal to Monoclinic Phase Transformation at Room Temperature in $Ba_xFe_{2x}Ti_{8-2x}O_{16}$ Hollandite due to Increased Ba Occupancy. *Mater. Res. Bull.* **2004**, *39*, 1075−1081.
(21) Carter, M. L.; Withers, R. L. A Universally Applicable Composite Modulated Structure Approach to Ordered $Ba_xM_yTi_{8-y}O_{16}$ Hollandite-type Solid Solutions. *J. Solid State Chem.* **2005**, *178*, 1903−1914.
(22) Moetakef, P.; Larson, A. M.; Hodges, B. C.; Zavalij, P.; Gaskell, K. J.; Piccoli, P. M.; Rodriguez, E. E. Synthesis and crystal chemistry of microporous titanates $K_x(Ti,M)_8O_{16}$ where M = Sc-Ni. *J. Solid State Chem.* **2014**, *220*, 45−53.
(23) Guo, Z.-Q.; Miao, N.-X.; Zhou, J.-P.; Lei, Y.-X.; Hassan, Q. U.; Zhou, M.-M. Novel magnetic semiconductor $Na_2Fe_2Ti_6O_{16}$: Synthesis, double absorption and strong adsorptive ability. *J. Mater. Chem. A* **2017**, *5*, 17589−17600.
(24) Knyazev, A. V.; Chernorukov, N. G.; Ladenkov, I. V.; Belopol'skaya, S. S. Synthesis, Structure, and Thermal Expansion of $M_2Fe_2Ti_6O_{16}$ and $MFeTiO_4$ Compounds. *Inorg. Mater.* **2011**, *47*, 999−1005.
(25) Hassan, Q. U.; Yang, D.; Zhou, J. P.; Lei, Y. X.; Wang, J. Z.; Awan, S. U. Novel Single-Crystal Hollandite $K_{1.46}Fe_{0.8}Ti_{7.2}O_{16}$ microrods: Synthesis, Double Absorption, and Magnetism. *Inorg. Chem.* **2018**, *57*, 15187−15197.
(26) Stitzer, K. E.; Smith, M. D.; Gemmill, W. R.; zur Loye, H.-C. Novel Mixed-Valent (V/VI) triple perovskite ruthenates: Observation of a complex low-temperature structural and magnetic transition. *J. Am. Chem. Soc.* **2002**, *124*, 13877−13885.
(27) Morrison, G.; Latshaw, A. M.; Spagnuolo, N. R.; zur Loye, H.-C. Observation of intense X-ray scintillation in a family of mixed anion silicates, $Cs_3RESi_4O_{10}F_2$ (RE = Y, Eu-Lu), Obtained via an enhanced flux crystal growth technique. *J. Am. Chem. Soc.* **2017**, *139*, 14743−14748.
(28) Latshaw, A. M.; Morrison, G.; zur Loye, K. D.; Myers, A. R.; Smith, M. D.; zur Loye, H.-C. Intrinsic blue-white luminescence, luminescence color tunability, synthesis, structure, and polymorphism of $K_3YSi_2O_7$. *CrystEngComm* **2016**, *18*, 2294−2302.
(29) Ferreira, T.; Morrison, G.; Chance, W. M.; Calder, S.; Smith, M. D.; zur Loye, H.-C. $BaFe_4O_7$ and $K_{0.22}Ba_{0.89}Fe_4O_7$: Canted antiferromagnetic diferrites with exceptionally high magnetic ordering temperatures. *Chem. Mater.* **2017**, *29*, 2689−2693.
(30) APEX3 Version 2016.5-0 and *SAINT*+ Version 8.37A; Bruker AXS, Inc.: Madison, Wisconsin, USA, 2016.
(31) SADABS-2016/2: Krause, L.; Herbst-Irmer, R.; Sheldrick, G. M.; Stalke, D. *J. Appl. Crystallogr.* **2015**, *48*, 3−10.
(32) (a) SHELXT: Sheldrick, G. M. *Acta Crystallogr., Sect. A: Found. Adv.* **2015**, *71*, 3−8. (b) SHELXL: Sheldrick, G. M. *Acta Crystallogr.* **2015**, *C71*, 3−8.
(33) ShelXle: a Qt graphical user interface for SHELXL: Hubschle, C. B.; Sheldrick, G. M.; Dittrich, B. *J. Appl. Crystallogr.* **2011**, *44*, 1281−1284.
(34) Kubelka, P.; Munk, F. Ein Beitrag zur Optik der Farbanstriche. *Z. Technol. Phys.* **1931**, *12*, 593.
(35) Morrison, G.; zur Loye, H.-C. Simple correction for the sample shape and radial offset effects on SQUID magnetometers: Magnetic measurements on Ln_2O_3 (Ln = Gd, Dy, Er) standards. *J. Solid State Chem.* **2015**, *221*, 334−337.
(36) Kresse, G.; Furthmüller, J. Efficient iterative schemes for ab initio total-energy calculations using a plane-wave basis set. *Phys. Rev. B: Condens. Matter Mater. Phys.* **1996**, *54*, 11169−11186.
(37) Kresse, G.; Furthmüller, J. Efficiency of ab-initio total energy calculations for metals and semiconductors using a plane-wave basis set. *Comput. Mater. Sci.* **1996**, *6*, 15−50.
(38) Perdew, J. P.; Burke, K.; Ernzerhof, M. Generalized gradient approximation made simple. *Phys. Rev. Lett.* **1996**, *77*, 3865−3868.

https://dx.doi.org/10.1021/acs.cgd.9b01560
Cryst. Growth Des. 2020, 20, 2398−2405

(39) Blöchl, P. E. Projector augmented-wave method. *Phys. Rev. B: Condens. Matter Mater. Phys.* **1994**, *50*, 17953−17979.
(40) Kresse, G.; Joubert, D. From ultrasoft pseudopotentials to the projector augmented-wave method. *Phys. Rev. B: Condens. Matter Mater. Phys.* **1999**, *59*, 1758−1775.
(41) van de Walle, A. Multicomponent multisublattice alloys, nonconfigurational entropy and other additions to the Alloy Theoretic Automated Toolkit. *CALPHAD: Comput. Coupling Phase Diagrams Thermochem.* **2009**, *33*, 266−278.
(42) Walle, A.; Ceder, G. Automating first-principles phase diagram calculations. *J. Phase Equilib.* **2002**, *23*, 348−359.
(43) van de Walle, A.; Asta, M.; Ceder, G. The alloy theoretic automated toolkit: A user guide, CALPHAD: Comput. *CALPHAD: Comput. Coupling Phase Diagrams Thermochem.* **2002**, *26*, 539−553.
(44) Walle, A.; Asta, M. Self-driven lattice-model Monte Carlo simulations of alloy thermodynamic properties and phase diagrams. *Modell. Simul. Mater. Sci. Eng.* **2002**, *10*, 521−538.
(45) Saal, J. E.; Kirklin, S.; Aykol, M.; Meredig, B.; Wolverton, C. Materials design and discovery with high-throughput density functional theory: The Open Quantum Materials Database (OQMD). *JOM* **2013**, *65*, 1501−1509.
(46) Kirklin, S.; Saal, J. E.; Meredig, B.; Thompson, A.; Doak, J. W.; Aykol, M.; Rühl, S.; Wolverton, C. The Open Quantum Materials Database (OQMD): assessing the accuracy of DFT formation energies. *npj Comput. Mater.* **2015**, *1*, 15010.
(47) Bugaris, D. E.; zur Loye, H.-C. Materials discovery by flux crystal growth: Quaternary and higher order oxides. *Angew. Chem., Int. Ed.* **2012**, *51*, 3780−3811.
(48) Juillerat, C. A.; Klepov, V. V.; Morrison, G.; Pace, K. A.; zur Loye, H.-C. Flux Crystal Growth: A Versatile Technique to Reveal the Crystal Chemistry of Complex Uranium Oxides. *Dalton Trans.* **2019**, *48* (10), 3162−3181.
(49) Mugavero, S. J.; Gemmill, W. R.; Roof, I. P.; zur Loye, H.-C. Materials Discovery by Crystal Growth: Lanthanide Metal Containing Oxides of the Platinum Group Metals (Ru, Os, Ir, Rh, Pd, Pt) from Molten Alkali Metal Hydroxides. *J. Solid State Chem.* **2009**, *182* (7), 1950−1963.
(50) Cotton, F. A.; Wilkinson, G.; Murillo, C. A.; Bochmann, M. *Advanced Inorganic Chemistry*; Wiley: New York, 1999.
(51) Rijssenbeek, J. T.; Matl, P.; Batlogg, B.; Ong, N. P.; Cava, R. J. Electrical and Magnetic Properties of a Series of Ternary Barium Metal Ruthenates: $Ba_3MRu_2O_9$ (M = Fe, Co, Ni, Cu, and In). *Phys. Rev. B: Condens. Matter Mater. Phys.* **1998**, *58* (16), 10315−10318.
(52) Middey, S.; Ray, S.; Mukherjee, K.; Paulose, P. L.; Sampathkumaran, E. V.; Meneghini, C.; Kaushik, S. D.; Siruguri, V.; Kovnir, K.; Sarma, D. D. Glasslike Ordering and Spatial Inhomogeneity of Magnetic Structure in $Ba_3FeRu_2O_9$: Role of Fe/Ru Site Disorder. *Phys. Rev. B: Condens. Matter Mater. Phys.* **2011**, *83* (14), 144419.

https://dx.doi.org/10.1021/acs.cgd.9b01560
Cryst. Growth Des. 2020, 20, 2398−2405